https:// doi.org/10.1007/s40145-019-0354-0

Research Article

Combined quantitative microscopy on the microstructure and phase evolution in $Li_{1.3}Al_{0.3}Ti_{1.7}(PO_4)_3$ ceramics

Deniz Cihan GUNDUZ[a,b,c,*], Roland SCHIERHOLZ[a,*], Shicheng YU[a], Hermann TEMPEL[a], Hans KUNGL[a], Rüdiger-A. EICHEL[a,b,c]

[a]*Forschungszentrum Jülich, Institute of Energy and Climate Research (IEK-9: Fundamental Electrochemistry), D-52425 Jülich, Germany*

[b]*Forschungszentrum Jülich, Institute of Energy and Climate Research (IEK-12: Helmholtz-Institute Münster: Ionics in Energy Storage), D-48149 Münster, Germany*

[c]*RWTH Aachen University, Institute of Physical Chemistry, D-52074 Aachen, Germany*

Received: May 12, 2019; Revised: October 05, 2019; Accepted: November 2, 2019

* Corresponding authors.

E-mail address: D. C. Gunduz, deniz.guenduez@rwth-aachen.de;

R. Schierholz, r.schierholz@fz-juelich.de

Abstract

Lithium aluminum titanium phosphate (LATP) is one of the materials under consideration as an electrolyte in future all-solid-state lithium-ion batteries. In ceramic processing, the presence of secondary phases and porosity play an important role. In a presence of more than one secondary phase and pores, image analysis must tackle the difficulties about distinguishing between these microstructural features. In this study, we study the phase evolution of LATP ceramics sintered at temperatures between 950 and 1100 ℃ by image segmentation based on energy-dispersive X-ray spectroscopy (energy disperse spectroscopy, EDS) elemental maps combined with quantitative analysis of LATP grains. We found aluminum phosphate ($AlPO_4$) and another phosphate phase ($(Li_x)P_yO_z$). The amount of these phases changes with sintering temperature. First: Since the grains act as an aluminum source for $AlPO_4$ formation, the aluminum content in the LATP grains decreases. Second: the amount of secondary phase changes from more $(Li_x)P_yO_z$ at 950 ℃ to mainly $AlPO_4$ at 1100 ℃ sintering temperature. We also used

scanning electron microscopy and confocal laser scanning microscopy to study the evolution of the LATP grains and $AlPO_4$, and LATP grain size increases with sintering temperature. In addition, transmission electron microscopy (TEM) was used for the determination of grain boundary width and to identify the amorphous structure of $AlPO_4$.

Keywords: Lithium aluminum titanium phosphate (LATP); microstructure; quantitative microscopy; grain size; confocal laser scanning microscopy (CLSM); NASICON

1 Introduction

Inorganic solid Li-conducting electrolytes are considered as potential candidates for next-generation Li-ion batteries, allowing to overcome key limitations of current technology associated with the use of the organic liquid electrolytes, such as flammability and electrochemical instability [1]. Developing solid electrolytes of Li-ion conductivity comparable to state-of-the-art liquid electrolytes with conductivities greater than 1 mS/cm; however, is a multi-scale challenge [2]. Criteria to tailor charge-transport properties in solids extends from atomic-scale properties [3,4] over microstructural features related to intergranular contact [5] and secondary-phase formation [6,7] to interface issues in the full battery cell [8]. Various types of Li-ion conducting solid-state electrolytes have been reported in Ref. [9]. Promising ionic conductivities have been reported for Li_3N [10], perovskite-type $La_{2/3-x}Li_xTiO_3$ [11], garnet type $Li_7La_3Zr_2O_{12}$ [12,13], thio LISICON-type $Li_{10}GeP_2S_{12}$ [14], B_2S_3–Li_2S–LiI glass [15], and NASICON-type $Li_{1+x}M_xTi_{2-x}(PO_4)_3$ [6,16].

Focusing on solid electrolytes that can be processed under dry-room conditions, NASICON-type $Li_{1+x}M_xTi_{2-x}(PO_4)_3$ are the materials of choice, as they combine high Li-ion conductivity with stability under air [17] and electrochemical stability window from 2.17 to 4.21 V [18]. The ionic conductivity of the pure compound $LiTi_2(PO_4)_3$; however, is too low to be employed in an all-solid-state cell. Aono *et al.* [6,16] demonstrated that partially substituting Ti with trivalent metal ions, $Li_{1+x}M_xTi_{2-x}(PO_4)_3$ (M = Al, Sc, Y, La, Ga, Fe, In, Lu, or Cr) enhances the conductivity for x around 0.3 for all M^{3+} ions except for Cr. Such a substitution affects both on the ionic conductivity within the crystal structure [19] and the microstructure of the ceramic pellet [7,16,20,21]. The conduction pathways in the NASICON structure was elucidated with neutron scattering [19]. Recently, the increase in Li-ion conductivity on substituting Ti by Al in $Li_{1+x}Al_xTi_{2-x}(PO_4)_3$ was shown independently on microstructural effects on single crystals by using micro-contacting reaching a maximum at x = 0.4, where x was tracked via atomic emission spectroscopy [22]. A recent review by Xiao *et al.* [23] gives an overview of the literature published on

LATP. For the present material, impedance measurements give a grain ionic conductivity that exceeds the grain-boundary ionic conductivity by almost three orders of magnitude [24].

The influence of processing parameters and secondary phases on the ionic conductivity was studied by many groups [7,20,21,25,26]. Crack formation in LATP grains was mainly observed in larger grains and at higher sintering temperatures by Hupfer *et al.* [20]. Cracks were found to originate at the interface of LATP grains and $AlPO_4$ secondary phase by *Waetzig et al.* [26]. Hupfer *et al.* [21] also studied the influence of the addition of small amounts of $LiTiOPO_4$ to LATP and LTP ($LiTi_2(PO_4)_3$) on the microstructure. They found 5% addition of $LiTiOPO_4$ as an optimum to reduce the amount of $AlPO_4$ secondary phase, but not fully suppressing the secondary phase formation to still benefit from it as it aids on densification and inhibits abnormal grain growth. Aono *et al.* [16,27] reported the increased densification by adding Li salts (Li_3PO_4, Li_2O, $Li_2P_4O_7$) to $LiTi_2(PO_4)_3$ and LATP. Infiltration of LATP with ionic liquid (IL) increases the ionic conductivity, and the interaction between grain boundary and IL was held responsible for that [28]. Also, $LiPO_3$ and Li_2SO_4 [29], $Li_{2.9}B_{0.9}S_{0.1}O_{3.1}$ [30], and LiF [31] aids in increasing ionic conductivity.

The use of combined microscopy for the investigation of LATP ceramics was reported via a correlative scanning electron microscopy (SEM) and electrochemical strain microscopy (ESM) approach on a local scale [32]. However, the overall microstructure and phase composition of LATP change with sintering temperature; therefore, techniques on a larger scale are needed for LATP ceramics sintered at different temperatures. Here, we report on a combined quantitative microscopic study employing SEM, CLSM, TEM, and EDX (SEM and STEM) as well as a novel image segmentation and reconstruction method to investigate the sintering temperature-dependent microstructure and phase evolution of LATP ceramics.

2 Materials and methods

2.1 Pellet fabrication

LATP-powders were synthesized by an oxalic acid supported conventional sol–gel method [7]. In the synthesis route, 25 mL of $Ti(OC_3H_8)_4$ (⩾ 97.0%) was mixed with 50 mL NH_4OH (Sigma–Aldrich, 28%–30% solution) in a beaker, which then produced a white gelatinous precipitate. The precipitate was cleaned with a large amount of deionized water to get rid of the excess base and put into 100 mL of deionized water (⩾ 99.9%). 200 mL of 1M oxalic acid (Sigma–Aldrich, 99.9%) was added into this solution, which produced a clear solution of $H_2[TiO(C_2O_4)_2]$. Stoichiometric $Al(NO_3)_3{\cdot}9H_2O$ (⩾ 98.0%)(Sigma-Aldrich), $(NH_4)_2HPO_4$ (⩾ 98.0%)(Sigma-Aldrich) and 5% excess $LiCOOCH_3{\cdot}2H_2O$ (⩾ 98.0%)(Sigma-Aldrich) were

dissolved in water added into the $H_2[TiO(C_2O_4)_2]$-solution in a slow manner so as to clear it under stirring. The final solution was then heated on a hot plate at 60 ℃ overnight under very strong stirring. Finally, the temperature was elevated to 140 ℃ until the evaporation of water takes place giving a white precipitate of well-mixed precursors for annealing. Afterward, precursors were ground. The mixture was then pre-annealed in the air for 5 h at 850 ℃ with a heating rate of 100 ℃ per hour. Holding time and heating rate was optimized according to phase purity and lithium ion loss.

The pre-annealed powder was first ground, filled into dies and uniaxially pressed to cylindrical pellets of 11 mm diameter with 40 kN. Subsequently, the pellets were densified by cold isostatic pressing for 10 s at 1425 kN. The pellets were then sintered in the air for 8 h in an alumina crucible ("Alsint 99.7" Morgan Advanced Materials, with 99.7% purity, the difference are mainly MgO and SiO_2) at different temperatures from 950 to 1100 ℃ in 50 ℃ steps. Ceramic pellets were covered with a parent powder in order to avoid from lithium-ion loss as well as contamination from the crucible.

2.2 Grinding and polishing procedure

Pellets were ground and polished to obtain well defined polished sections. Initially, samples were ground with 15, 10, and 5 µm silicon carbide (SiC) sandpapers, in the respective order with a commercially available oil-based lubricant solution (Cloeren Technologies). Subsequently, polishing was applied with oil-based diamond suspensions with particle sizes of 3 and 1 µm (Buehler, MetaDi, oil-based). In the last polishing step, a water-free suspension of a blend of high-purity alumina and colloidal silica with a particle size of 0.05 µm (Buehler, MasterPolish) was used.

2.3 Microscopy

2.3.1 Confocal laser scanning microscopy

A 3D measuring confocal laser scanning digital microscope (CLSM) (Olympus LEXT OLS4100, Japan) was employed to carry out microstructural investigations on polished samples. High-resolution images were recorded with the 50x and 100x objective lenses, which both have a numerical aperture of 0.95.

2.3.2 Scanning electron microscopy

Samples were analyzed using SEM (Quanta FEG 650; FEI part of Thermo Fischer, Hillsboro, Oregon, USA) equipped with field emission gun (FEG) and energy-dispersive X-ray spectroscopy (EDS) (Octane 60 mm^2, EDAX Inc., Mahwah, NJ, USA).

2.3.3 Lamella preparation

Lamellas for TEM and STEM-EDS were cut out of an SEM sample and thinned with a Helios Nanolab 460 F1 (FEI part of Thermo Fischer, Hillsboro, Oregon, USA) [33].

2.3.4 Transmission electron microscopy

TEM experiments were conducted at 200 kV with a Tecnai G2 F20 (FEI part of Thermo Fisher, Hillsboro, Oregon, USA) [34].

2.3.5 Scanning transmission electron microscopy–EDS

Scanning transmission electron microscopy with EDS–mapping was conducted on a Titan Crewley 80-200 (FEI part of Thermo Fischer, Hillsboro, Oregon, USA) operated at 80 kV [35].

2.4 Image analyses

Segmentation of the different phases from single EDS elemental maps was carried out with the image analysis program Avizo 9 (FEI Visualization Sciences Group, FEI, Hillsboro, Oregon, USA).

We used Avizo also for the segmentation of CLSM and SEM micrographs and chose the thresholds such that the darker levels cover the lower regions, the bright levels cover the grains, and the intermediate levels cover the secondary phase. Grains were separated with the separate objects module based on a watershed algorithm, and also manual corrections were applied for this purpose when they are necessary. Analysis Filter module was used to eliminate noise by excluding very small objects. Grains that are not fully inside of the analysis area were excluded from the analysis. The size of the grains reported here was retrieved via taking the square root of grain areas.

3 Results and discussion

3.1 Phase identification and attribution by SEM/STEM-EDS

In this part, we investigate how many and which phases are present in the sections of the material. For this, we first used SEM imaging with EDS point analyses as shown exemplarily in Fig. 1. This shows two backscatter electron (BSE) micrographs for LATP samples sintered at 1100 (left) and 1050 ℃ (right). For the 1100 ℃ sample, three different gray levels can be obtained, and point spectra reveal three different phases, with the elemental quantification given in Table 1. As Li cannot be detected and quantified by EDS, we also provide theoretical values excluding Li.

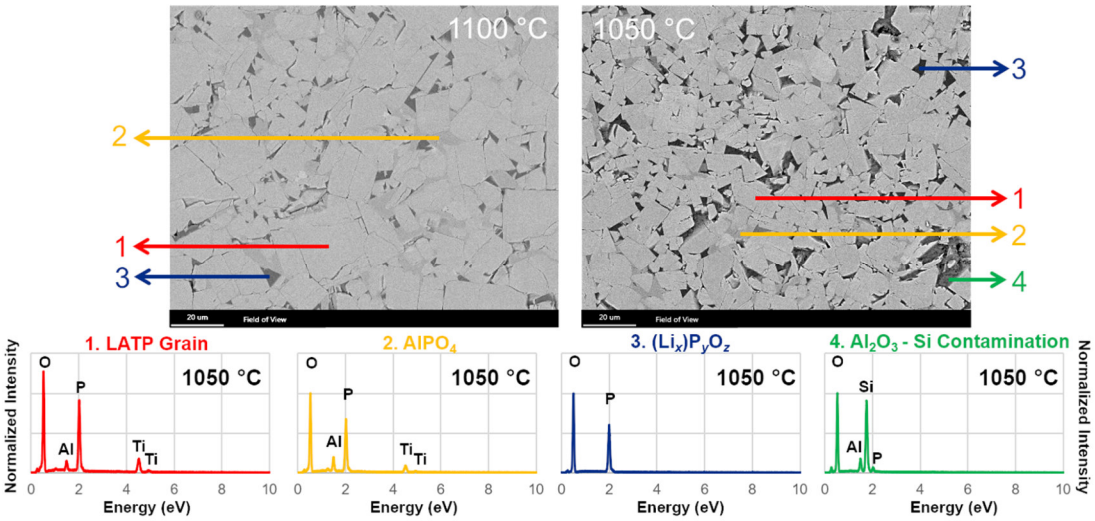

Fig. 1 SEM micrographs of LATP samples sintered at 1050 and 1100 ℃ and point spectra from the marked positions of the 1050 °C sample are given underneath. The same phase components are also marked in the 1100 ℃ sample as an illustration.

Table 1 Quantification of spectra from points 1 to 3 in both images in Fig. 1 and the three regions marked in Fig. 2. For comparison, theoretical values are given for $(Li_4)P_2O_7$ and $(Li_3)PO_4$ excluding Li as well as for $(Li_{1.3})Al_{0.3}Ti_{1.7}(PO_4)_3$ and $AlPO_4$. Elemental ratios were provided at the right side

SEM 1100 ℃	Al	Ti	P	O	c_{Al}/c_{Ti}	c_P/c_{Ti}	c_O/c_P
Point 1	1.89	11.57	20.91	65.63	0.16	0.55	3.14
Point 2	4.93	8.08	20.71	66.28	—	—	3.2
Point 3	—	—	23.9	76.1	—	—	3.18
SEM 1050 ℃	Al	Ti	O	P	c_{Al}/c_{Ti}	c_P/c_{Ti}	c_O/c_P
Point 1	2.05	11.93	21.32	64.71	0.17	0.56	3.04
Point 2	4.29	8.55	21.99	65.17	—	—	2.96
Point 3	—	—	27.94	72.06	—	—	2.58
Theoretical	Al	Ti	P	O	c_{Al}/c_{Ti}	c_P/c_{Ti}	c_O/c_P
$(Li_{1.3})Al_{0.3}Ti_{1.7}(PO_4)_3$	1.76	10.00	17.65	70.59	0.18	0.57	4
$AlPO_4$	16.67	0.00	16.67	66.67	—	—	4
$Li_4P_2O_7$	—	—	22.22	77.78	—	—	3.5
$(Li_3)PO_4$	—	—	20	80	—	—	4
STEM	Al	Ti	P	O	c_{Al}/c_{Ti}	c_P/c_{Ti}	c_O/c_P
950 ℃ Area 1 ($AlPO_4$)	17.57	0.02	17.16	65.25	—	—	3.8
950 ℃ Area 2 (LATP)	2.28	11.52	20.67	65.52	0.2	0.56	3.17
1050℃ Area 3 ($Li_xP_yO_z$)	0.09	0.02	21.07	78.82	—	—	3.74

The quantification of the spectra at point 1 inside the grains in both samples gives values of about 2 at% Al, 12 at% Ti, 21 at% P, and 66 at% O. The values for Al, Ti and P are higher than the theoretical values, and the content of O is lower. This can be attributed to the emission line energies. O Kα (0.525 keV) has a very low emission line energy compared to the other elements (Al Kα: 1.486 keV, Ti Kα: 4.510 keV, and P Kα: 2.010 keV) and suffers from absorption, which we did not correct for. Looking at the elemental ratios, the $\frac{c_{Al}}{c_{Ti}}$ ratio inside the LATP grains is close to the theoretical value of 0.18. The $\frac{c_O}{c_P}$ ratio

is close to or varies between 3 and 3.2, which we attribute partly to the absorption of the O Kα emission line. Within the experimental error, we can attribute the grains to crystalline $Li_{1.3}Al_{0.3}Ti_{1.7}(PO_4)_3$ with $R\bar{3}c$ crystal structure (ICSD No. 427619) [36] according to previously reported X-ray powder diffraction results of the same material [7].

Coming to the secondary phase regions, the quantification of point 2 in the light gray secondary phase clearly exhibits higher content of Al and a reduced amount of Ti compared to the grains (Table 1). For the secondary phases, the influence of the excitation/escape volume comes even more into account. Ti with Kα emission line at ~4.5 KeV is expected to have the largest volume and the amount of Ti will be rather overestimated, as Ti Kα emission lines can be excited in and escape from neighboring as well as underlying LATP grains. For O with Kα emission line at ~0.525 keV, this is rather the opposite. O is only detectable close to the surface. Unfortunately, Ti L emission lines overlap with the O Kα emission lines impeding a quantification based only on Ti Lα and O Kα emission lines. With the acceleration voltage of 10 keV and Ti Kα emission line used for the quantification, the intensity of Ti in this secondary phase could arise from neighboring and/or underlying grains as the secondary phases exhibit lower absorption coefficients. The secondary phase in point 2 can be attributed to $AlPO_4$ even though the quantification of SEM-EDS spectra gives deviating results, with some Ti content and the $\frac{c_O}{c_P}$ ratio differing from 4. The quantitative analysis of area 1 in the STEM–EDS map (Fig. 2) matches well with $AlPO_4$ within the experimental error. TEM and STEM only show amorphous contrast for this secondary phase.

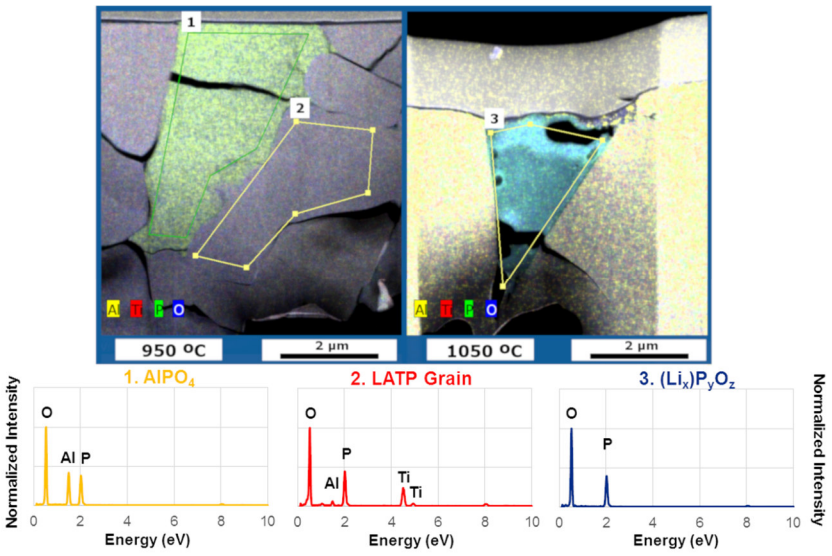

Fig. 2 Local STEM-EDS elemental phase maps of LATP samples sintered at 950 and 1050 ℃. Spectra extracted from three regions are displayed at the bottom and with the quantification given in Table 1.

Point 3 in both SEM images in Fig. 1 only shows O Kα and P Kα emission lines in the spectrum. As Li is not detectable by EDS, no conclusion can be drawn whether Li is present in this secondary phase, but a (lithium) phosphate is probable. The $\frac{c_O}{c_P}$ ratio ranges from close to 3.2 for LATP 1100 ℃ to 2.5 for LATP 1050 ℃, so different (lithium) phosphates are probable. The scattering of quantified values and the problems in the determination of the absolute $\frac{c_O}{c_P}$ ratio due to absorption effects make a clear assignment difficult. For the area 3 in the STEM-EDS map of the sample sintered at 1050 ℃ in Fig. 2, a quantification leads to a $\frac{c_O}{c_P}$ ratio of 3.75 between 3.5 as expected for $Li_4P_2O_7$ and 4 as expected for Li_3PO_4. Aono *et al.* [6] mention $Li_4P_2O_7$ and LiO_2 as decomposition products if Li salts are added as binders. In our case, $Li_4P_2O_7$ is possible as well as any other phosphates such as Li_3PO_4.

The spectrum of point 4 in the 1050 ℃ sample shows only a weak P signal and instead Al, Si, and O signals, which can be attributed to polishing particles accumulating in this area. These particles were found in some areas by higher magnification SEM. This shows that thresholding the images for segmentation of SEM micrographs is sensitive to errors and artifacts, as it is especially difficult to separate the dark gray secondary phase, pores, and pores partially filled by the polishing material.

As SEM–EDS quantification suffers from the difference in excitation/escape volume for the different elements impeding a quantification/phase assignment, we performed additional STEM–EDS on a focused ion beam cut TEM–lamella of samples sintered at 950 and 1050 ℃. Fig. 2 shows the overlay of the Al, Ti, P, and O maps on the HAADF-images (single EDS elemental maps are not shown). These three different regions can be clearly distinguished in consistency with SEM observations. Three areas as marked in Fig. 2 have been picked for quantitative analysis of the spectra. Results are given in Table 1 underneath the SEM-quantification. For the grain, similar deviations from the nominal composition are observed as in SEM confirming these results. Quantification of the Al-rich area gives results matching very well with $AlPO_4$. In contrast to SEM–EDS, the same holds for the quantification of the spectra belonging to the third phase containing mainly P and O. The $\frac{c_O}{c_P}$ ratio here with 3.8 is close to the expected value of 4. Li could be present; however, we were not able to detect it due to the limitations of EDS. Therefore, we assume that the third phase is a lithium-containing phosphate [37], which we will refer to as $(Li_x)P_yO_z$ in the rest of the manuscript. Also, some amount of Al may be present in this approximately amorphous phase. Small amounts of elemental impurities such as K^+ and Mg^{2+} were observed in some phase regions. K^+, Mg^{2+}, and Al^{3+} in phosphate glasses have been reported [38,39].

3.2 Correlative EDS map and point spectra analysis of LATP

Similar to the three different regions in the STEM–EDS elemental maps, EDS elemental maps obtained in SEM providing a larger field of view can be used for quantitative phase analysis. Elemental maps for Al, Ti, P, and O were recorded at 10 kV to enable mapping of these elements using Al Kα (1.486 keV), Ti Kα (4.510 keV), P Kα (2.010 keV), O Kα (0.525 keV) emission lines, avoiding deconvolution of Ti Lα ($L\alpha_1$ 0.452 and O Kα (0.525) emission lines [40]. From these elemental maps, phase maps were reconstructed using the method depicted in Fig. 3 exemplarily for the LATP sample sintered at 1000 ℃. Elemental maps shown in the left column of Fig. 3 (O: cyan, P: yellow, Al: green, and Ti: red) were segmented into low (cyan), medium (magenta) and high-intensity (yellow) regions, representing low, medium, and high elemental content as shown in the center column of Fig. 3. Therefore, there are potentially three different regions exhibiting different intensities for each of the four elements, which can be taken into consideration to attribute the regions to different phases. In case of uncertainty in one elemental map, the Avizo software allows to cross-check with all other elemental maps as well as the secondary electron and backscatter electron micrographs. This allows the attribution according to Table 2.

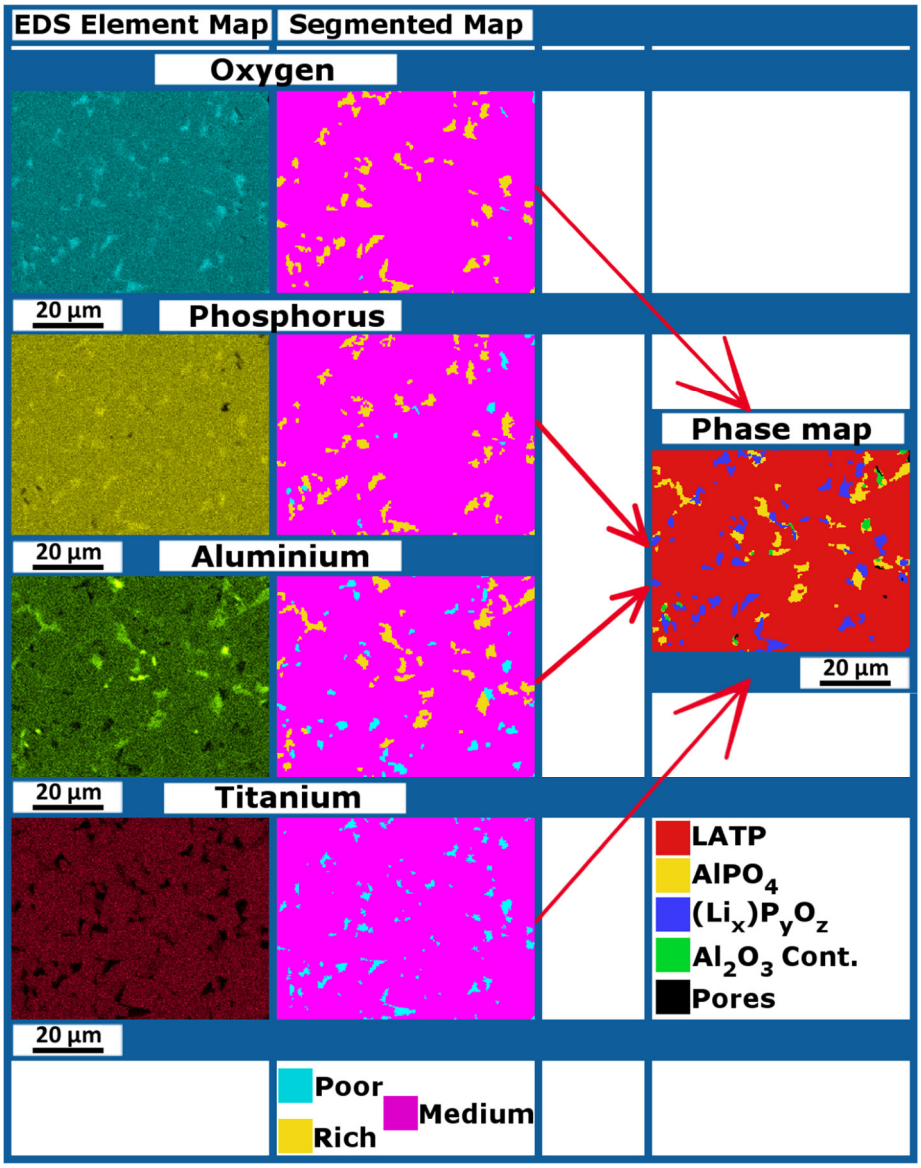

Fig. 3 SEM–EDS elemental maps of LATP sample sintered at 1000 ℃ (left column). Segmentation of each elemental map into regions with poor (cyan), medium (magenta), and rich (yellow) elemental content (center column). Phase map generated from the image analysis of single elemental maps (right column).

Table 2 Summary of how phases and/or regions were assigned to poor, medium, and rich regions in the elemental maps

Phases and/or regions	O	P	Al	Ti
LATP	Medium	Medium	Medium	Medium
$AlPO_4$	Medium	Medium	Rich	Medium
$(Li_x)P_yO_z$	Rich	Rich	Poor	Poor
Al_2O_3 polishing particles	Not Poor	Poor	Rich	Poor
Pores	Poor	Poor	Poor	Poor

The O-map shows mainly medium intensity, with some regions displaying high and only a few with low intensity. The P-map looks similar. $(Li_x)P_yO_z$ secondary phase appears with high intensity in the O-maps and P-maps. In a similar manner, $AlPO_4$ appears with high intensity in the Al-maps. The largest part in all maps shows the medium intensity and can be attributed to LATP. O-maps also represent the surface and pores well; therefore, the low intensity regions in the O-maps were used to identify pores. No regions were found showing only high intensity for Ti and O, which would be attributed to TiO_2, which is reported in Refs. [21,26]. Sometimes high intensity in the Al-map and medium/high intensity in the O-map can be observed while Ti and P only show low intensity. This is mostly observed at pore edges and can be attributed to Al_2O_3 residual polishing particles trapped there, which have not been washed away after polishing. Grain boundaries were not included as a separate phase in EDS elemental analyses, as their width is about 10 nm, and they cannot be resolved in EDS-mappings recorded at 10 kV. With the Eq. (1) [41], the excitation volume for LATP with a density ρ_{LATP} = 2.8 g/cm³, the atomic weight A = 383.4 g/mol and average Z = 10.2 can be calculated for an accelerating voltage E_0 = 10 keV to be R_{KO} = 22.4 µm.

$$R_{\mathrm{KO}}\ (\mu\mathrm{m}) = \frac{0.0276A}{Z^{0.89}\rho}E_0^{1.67} \qquad (1)$$

As the grain boundaries are narrow, they will not contribute much to the total amounts of the different phases. Four different regions for each sintering temperature were analyzed (see the supplementary information for additional EDS elemental mappings). In total regions of 2640 µm² (950 ℃), 16,508 µm² (1000 ℃), 16,508 µm² (1050 ℃), and 16,508 µm² (1100 ℃) were analyzed. For each region, elemental maps of O, P, Al, and Ti were analyzed and phase maps were constructed. Higher magnification was used for the 950 ℃ sintering temperature since all secondary phase regions are relatively smaller at this temperature.

Exemplary final phase maps are shown in Fig. 4 for all sintering temperatures. Analyzing all the final phase maps, the overall quantitative phase content from all maps was extracted and is shown in Fig. 5. At 950 ℃, the amount of secondary phases is the lowest and the observed main secondary phase is $(Li_x)P_yO_z$ with ~5%. Only a little amount of $AlPO_4$ (1 %) is found for this sample. With increasing sintering temperature, the amount of $(Li_x)P_yO_z$ decreases, while more $AlPO_4$ is found. Between 1000 and 1050 ℃, the main secondary phase changes from $(Li_x)P_yO_z$ to $AlPO_4$. A strong step is then observed in the last step from 1050 to 1100 ℃, in which the amount of $(Li_x)P_yO_z$ decreases from 3.2 % to 1.7% and the amount of $AlPO_4$ increases from 5.1% to 8.8%. The total amount of secondary phases increases as well with sintering temperature. A similar trend is observed for the porosity, but here a maximum is observed at

1050 ℃, which is also the temperature we detected the polishing particles. At other temperatures, we detected much less of these residual polishing particles. Hence, the quantification of porosity at this temperature should be treated with care. First increasing, and the final step decreasing porosity might arise due to the initial dissolution and final densification processes of Ostwald ripening. Ostwald ripening leads to grain growth through the consumption of smaller grains by new or already existing larger ones [42], which goes in par with our observation of increasing grain sizes with the increasing sintering temperature. During the course of Ostwald ripening, an increase in the average pore size accompanies the increase in the average grain size of the system [43]. On the other hand, this correlation between the average grain size and the average pore size may also suggest that pores are relatively smaller at relatively lower temperatures and might not be fully detected via employing this method.

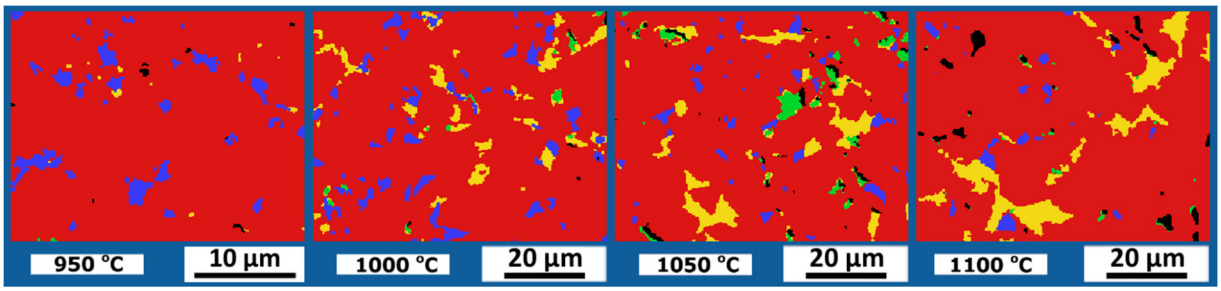

Fig. 4 Exemplary phase maps of LATP samples for the sintering temperatures of between 950 and 1100 ℃ obtained via the method described in Fig. 3 showing regions containing LATP in red, $AlPO_4$ in yellow, $(Li_x)P_yO_z$ in blue, residual polishing particles in green, and pores in black.

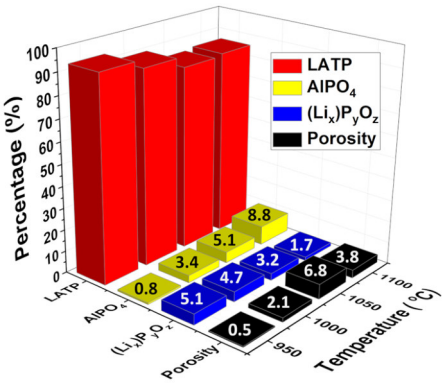

Fig. 5 Quantification of phases retrieved from all phase map analyses.

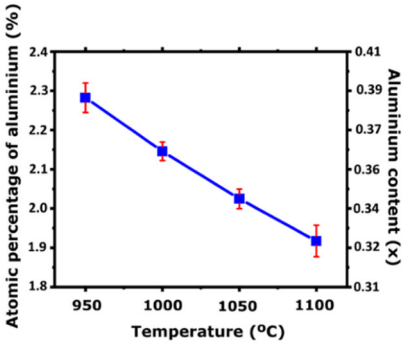

Fig. 6 Sintering temperature-dependent evolution of the atomic percentage of LATP grains retrieved from 20 grains for each sintering temperature. Grains were selected from the areas where EDS map analyses were also carried out.

$AlPO_4$ formation requires sources of Al and phosphate. LATP grains are the only possible source of Al for $AlPO_4$ formation in the material system at the beginning. That is why we also measured EDS-spectra of twenty grains from the analyzed maps for each sintering temperature. Figure 6 displays the atomic percentage of Al among the elements of LATP apart for Li (Al, Ti, P, and O) for all samples. The Al-content *x* decreases with increasing sintering temperature. This explains the source of Al in $AlPO_4$ formation mechanism. One can write the loss of Al inside the LATP grains according to Eq. (2) as following:

$$18\ Li_{1.3}Al_{0.3}Ti_{1.7}(PO_4)_3 \rightarrow 17\ Li_{1.2}Al_{0.2}Ti_{1.8}(PO_4)_3 + 2\ AlPO_4 + Li_3PO_4 \qquad (2)$$

Cracks were mainly reported at LATP grain-$AlPO_4$ secondary phase interface [26]. The decrease of Al-content in grain stoichiometry during $AlPO_4$ formation with increasing sintering temperature might be a factor contributing to this behavior. According to Eq. (2), Li_3PO_4 should also be formed (half the amount of $AlPO_4$). Li_3PO_4 has a lower melting point (1225 ℃) than $AlPO_4$ (2030 ℃) [44]. Li_3PO_4 and $AlPO_4$ form an eutectic system at $AlPO_4/Li_3PO_4 \approx 60/40$, which melts at 933 ℃ [44]. We assume that this liquid aids in densification upon sintering. On the other hand, the lower melting point of Li_3PO_4 suggests that it is less stable at higher temperatures. It is probable that some of the Li_3PO_4 is lost upon higher sintering temperatures, so we observe a decreasing amount of the $Li_xP_yO_z$ secondary phase with increasing sintering temperature. The consumption of Al and (lithium) phosphate during $AlPO_4$ secondary phase formation might also be held accountable for the decrease in the amount of $(Li_x)P_yO_z$ secondary phase.

3.3 Combined CLSM and SEM of LATP

For the more complete understanding of the sintering temperature-dependent microstructural evolution of LATP ceramics, CLSM, and SEM were used for grain and $AlPO_4$ analyses. In Figs. 7(a) and 7(b), correlative SEM (left) and CLSM (middle) micrographs from the same positions of the LATP sample sintered at 1050 °C are given. Both CLSM and SEM micrographs display the LATP grains with a bright contrast and $AlPO_4$ secondary phase with intermediate gray level contrast. Darker regions are also

present. Therefore, with the careful adjustment of the thresholds, it is possible to distinguish grains and the light gray secondary phase. Unlike EDS map analyses, second secondary phase ($(Li_x)P_yO_z$), pores, and polishing particles were not separately studied with these techniques. Some regions appearing black in CLSM appear dark gray in the SEM. By high-resolution SEM, polishing particles accumulated at pore edges could be identified in these regions (Fig. 7(c)). Therefore, the darkness of such regions in CLSM might arise because of the transparency of residual polishing particles against laser light.

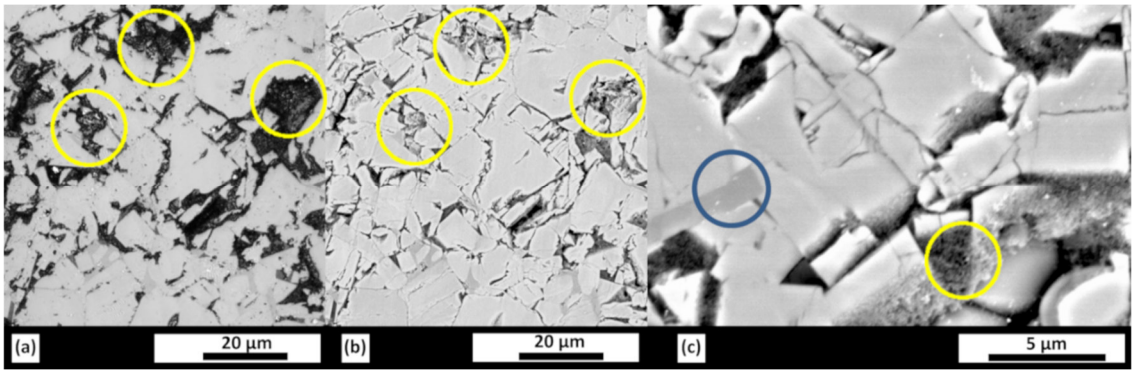

Fig. 7 Correlative SEM (left) and CLSM (middle) micrographs from the same positions of the LATP sample sintered at 1050 ℃. Some areas which appear quite dark in CLSM seem to contain material in SEM. At the right side, a higher-magnification SEM-micrograph of the same sample showing dense secondary phase in the blue circle and the accumulated polishing particles in the yellow circle.

Morphologically, $AlPO_4$ secondary phase appears intergranular, which is rather an evidence for an amorphous structure in contrast to the findings by XRD [7]. In the blue circle in Fig. 7(c), it seems still well connected to the surrounding grains, so it might aid in the densification of the material as discussed in Refs. [15,18,20]. Cracks within LATP grains are also observed in grains that are not directly connected to $AlPO_4$. In TEM, amorphous regions in triple points were observed frequently as shown for LATP 1000 ℃ in Fig. 8(a) and seem mostly well connected to grains. Also, part of the grain boundary shows a thin film with amorphous contrast in high-resolution (HR) TEM micrographs as shown in Fig. 8(b). Therefore, depending on SEM and HRTEM findings, it can be concluded that impurities are prone to form around grain boundary and the intergranular space. Grain boundaries vary in width, and according to the poor statistics in TEM, no significant difference in grain boundary width could be observed between the different samples. Especially for the higher sintering temperatures with larger grain sizes, only a part of a single grain boundary can be investigated per TEM sample. Furthermore, the preferential etching of grain boundaries during TEM sample preparation is a problem. Hence, we cannot give quantitative values for the grain boundary width distributions. Neither we can give values which amount of the grain boundary is wetted. As can be seen in Fig. 8(a), the film does not occur along the full length of this grain

boundary neither in the grain boundary in the lower right part of Fig. 8(a). On the other hand, the grain boundary above the triple point in the upper right part shows such a film.

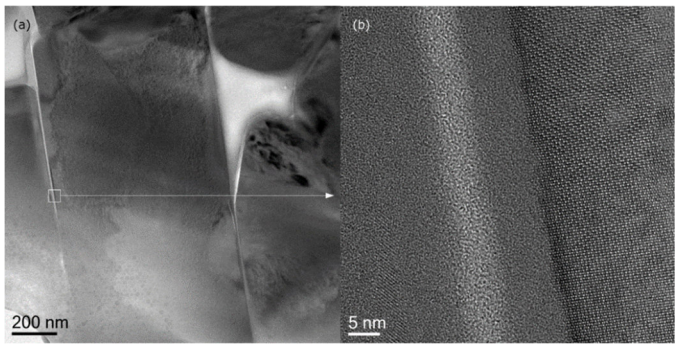

Fig. 8 (a) TEM-micrograph of LATP sintered at 1000 ℃ showing crystalline LATP grains and an amorphous secondary phase; (b) HRTEM-micrograph of the grain boundary in (a) revealing a thin amorphous region at the grain boundary.

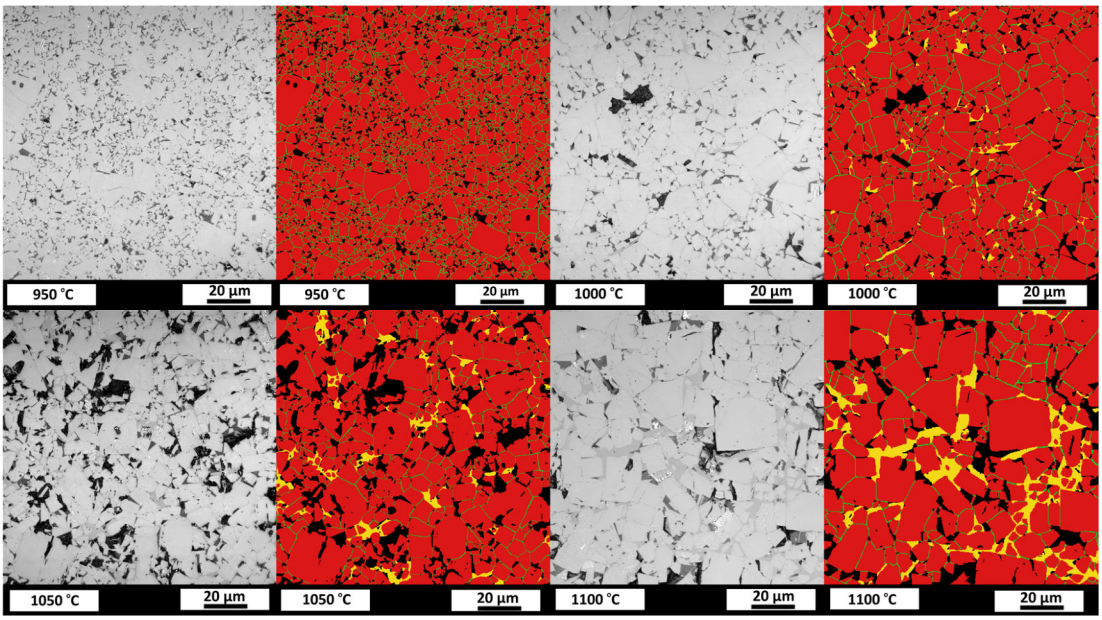

Fig. 9 CLSM micrographs of LATP samples for the sintering temperatures of between 950 and 1100 ℃ and their segmentation. Grains, grain boundaries, secondary phase, and pores are shown in red, green, yellow, and black, in the respective order. All micrographs are displayed in the same magnification.

Table 3 Results of the image analysis from CLSM (top) and SEM (bottom)

Sintering temperature (℃)	Mean grain size (µm)	σ (µm)	Grain symmetry	Number of grains analyzed	$AlPO_4$ (%)	Area analyzed (µm²)
950	1.59	1.87	0.75±0.11	3799	—	32338
1000	2.77	1.96	0.79±0.09	1230	1.7	32338
1050	3.29	2.08	0.78±0.10	356	3.9	16169
1100	4.88	2.10	0.77±0.10	672	7.2	65333
Sintering temperature(℃)	Mean grain size (µm)	σ(µm)	Grain symmetry	Number of grains analyzed	$AlPO_4$ (%)	Area analyzed (µm²)
950	1.52	1.80	0.85±0.06	284	—	1962

1000	2.56	2.09	0.82±0.07	257	1.9	7155
1050	3.35	2.12	0.76±0.12	634	3.2	28649
1100	5.01	2.10	0.81±0.08	329	6.4	28649

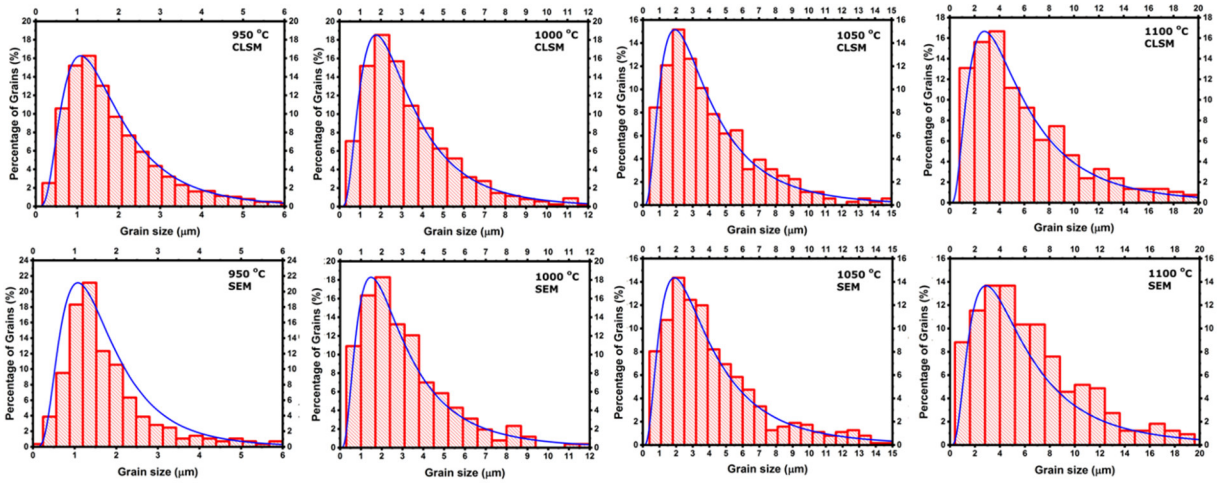

Fig. 10 Grain size distributions given with their percentages retrieved from CLSM and SEM image analyses for the sintering temperatures of between 950 and 1100 °C. Experimental values and log-normal fits are shown in red and blue, respectively. Mean values and σ for the log-normal distributions are given in Table 3.

Figure 9 shows CLSM images and their segmentation by Avizo for the samples sintered at temperatures of between 950 and 1100 °C. The segmented images show LATP grains, $AlPO_4$ secondary phase, grain boundaries, and pores colored in red, yellow, green, and black, respectively. Quantitative results from the analysis of CLSM and SEM micrographs are given in the top and bottom parts of Table 3, respectively. The size of all microstructural components (grains, pores, and secondary phase) increases with increasing sintering temperature. The $AlPO_4$ secondary phase (light gray areas) can be resolved by SEM and CLSM for the sintering temperatures of 1000 °C and higher and is found mainly allocated in larger intergranular spaces. Thin films at the grain boundary could be present but are not detectable by CLSM. This would not affect the total amount of secondary phase significantly as the total area would not change significantly.

Grain size distributions extracted from the CLSM micrograph analyses are depicted in the top row of Fig. 10 exhibiting log-normal distributions with the mean grain sizes and standard deviations (σ) listed in Table 3. For the 950 ℃ sample, much of the area is covered by small grains below 2 μm; whereas, some larger grains are already present. At 1000 ℃, the distribution becomes broader and extends to much larger grain sizes with a mean grain size of 2.77 μm. For 1050 ℃, the grain size increases further but not much to a mean value of 3.29 μm. A more drastic increase is observed at 1100 ℃. The broadest grain size distribution is observed at this sintering temperature and the mean grain size jumps up to 4.88 μm. Table

3 also lists the area fractions of $AlPO_4$ secondary phase. The total amount but also the size of the light gray secondary phase regions increases with sintering temperature from about 2% for the 1000 ℃ sample to 4% and 7% for 1050 and 1100 ℃ samples, respectively. This analysis shows a similar trend along the lines of the findings based on EDS map analysis (3.4%, 5.1%, and 8.3%), within the experimental error. Grain size distributions determined by SEM are similar to the ones determined by CLSM and shown in the bottom row of Fig. 10. They both exhibit log-normal characteristics. Furthermore, like the trend observed by CLSM, a strong increase in grain size observed for the increase of sintering temperature from 950 to 1000 ℃ and also for the last step from 1050 to 1100 ℃. In all samples, larger grains exhibit cracks as already stated by Refs. [18,19]. The increase in the amount of $AlPO_4$ secondary phase with sintering temperature is in line with EDS results.

Grain morphology is one of the most critical factors influencing the mechanical properties of ceramic materials. A standardized general model accounting for the quantitative grain-shape analysis; however, is still missing, and for LATP, no specific model has been reported so far. Exploiting the CLSM and SEM micrographs of LATP, at first sight mainly cuboidal shaped grains are present. Hence, it is required to quantify how much these cuboidal looking grains deviate from the ideal cubes. In order to gain further insight into the shape of grains, the symmetry measurement function, *S*, in the Avizo software, is employed. Related geometric parameters are shown in Fig. 11. C represents the center of mass of the two-dimensional homogenous grain; $I_{\mathrm{a}}$and I_{b} are the two intersection points of a single line and grain boundary. The symmetry measurement function can be written in terms of the geometric parameters as following:

$$S(G) = \frac{1}{2}[1 + \mathrm{Min}_n(\frac{A_{\mathrm{min}}}{A_{\mathrm{max}}})] \qquad (3)$$

where *G* stands for the single grain, $A_{\mathrm{min}} = \mathrm{Min}(\overline{I_{\mathrm{a}}C}, \overline{I_{\mathrm{b}}C})$, $\mathrm{A}_{\mathrm{max}} = \mathrm{Max}(\overline{I_{\mathrm{a}}C}, \overline{I_{\mathrm{b}}C})$, and Min_n represents the minimum value operator over the angles $\vartheta_n \in [0, \pi]$. For the case of a fully symmetric shape, a square for this case, symmetry measurement function will be equal to one. On the other hand, it will decrease with an increase in asymmetry. For all sintering temperatures, values around 0.8 are obtained for the symmetry function from both CLSM and SEM micrographs. Hence, the grains are not ideally cubic, but no sintering temperature dependence is observed.

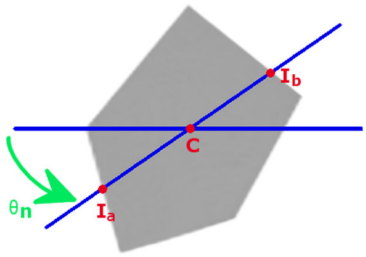

Fig. 11 Working mechanism of symmetry measurement is shown for a single grain.

4 Conclusions

In summary, the microstructural properties of LATP-pellets sintered at temperatures from 950 to 1100 ℃ with 50 ℃ steps were studied. In samples, crystalline LATP-grains, two amorphous secondary phases, $AlPO_4$, most probable a (lithium) phosphate $(Li_x)P_yO_z$, and pores are observed. Grain size, grain symmetry, and the amount of $AlPO_4$ are determined both by CLSM and SEM. Grain size and the amount of $AlPO_4$ increase with sintering temperature while grain symmetry does not change. An image analysis and reconstruction method based on EDS elemental maps revealed that with increasing temperature, $(Li_x)P_yO_z$ is consumed while more $AlPO_4$ is formed. Also, the correlative point spectra analyses from grains showed that Al-content inside the LATP grains is reduced because they act as Al source for the formation of $AlPO_4$ secondary phase. TEM results show that the $AlPO_4$ secondary phase is amorphous and not only filling larger intergranular regions but is also partially wetting grain boundaries with a few nm thin film. This can limit the ionic conductivity of samples. The second secondary phase $(Li_x)P_yO_z$ may contain Li and also provide better ionic conductivity. Therefore, higher content of this phase at the lower sintering temperatures might increase the ionic conductivity to some extent.

Acknowledgements

The FEI Helios NanoLab 460F1 and Quanta FEG 650 were funded by the German Federal Ministry of Education and Research (BMBF) via the project SABLE (SABLE-Skalenübergreifende, multi-modale 3D-Bildgebung Elektrochemischer Hochleistungskomponenten) under support code 03EK3543.

References

[1] Goodenough JB, Park KS. The Li-ion rechargeable battery: A perspective. *J Am Chem Soc* 2013, **135**: 1167–1176.
[2] Janek J, Zeier WG. A solid future for battery development. *Nat Energy* 2016, **1**: 16141.

[3] Jakes P, Granwehr J, Kungl H, *et al.* Mixed ionic–electronic conducting $Li_4Ti_5O_{12}$ as anode material for lithium ion batteries with enhanced rate capability–impact of oxygen non-stoichiometry and aliovalent Mg^{2+}-doping studied by electron paramagnetic resonance. *Z Phys Chem* 2015, **229:** 1439–1450.
[4] Wang Y, Richards WD, Ong SP, *et al*. Design principles for solid-state lithium superionic conductors. *Nat Mater* 2015, **14**: 1026–1031.
[5] Bates JB, Dudney NJ, Neudecker B, *et al.* Thin-film lithium and lithium-ion batteries. *Solid State Ion* 2000, **135:** 33–45.
[6] Aono H, Sugimoto E, Sadaoka Y, *et al.* Ionic conductivity of solid electrolytes based on lithium titanium phosphate. *J Electrochem Soc* 1990, **137:** 1023–1027.
[7] Yu S, Mertens A, Gao X, *et al*. Influence of microstructure and $AlPO_4$ secondary-phase on the ionic conductivity of $Li_{1.3}Al_{0.3}Ti_{1.7}(PO_4)_3$ solid-state electrolyte. *Funct Mater Lett* 2016, **9**: 1650066.
[8] Luntz AC, Voss J, Reuter K. Interfacial challenges in solid-state Li ion batteries. *J Phys Chem Lett* 2015, **6:** 4599–4604.
[9] Bachman JC, Muy S, Grimaud A, *et al.* Inorganic solid-state electrolytes for lithium batteries: Mechanisms and properties governing ion conduction. *Chem Rev* 2016, **116:** 140–162.
[10] Alpen UV, Rabenau A, Talat GH. Ionic conductivity in Li_3N single crystals. *Appl Phys Lett* 1977, **30**: 621–623.
[11] Inaguma Y, Chen L, Itoh M, *et al*. High ionic conductivity in lithium lanthanum titanate. *Solid State Commun* 1993, **86**: 689–693.
[12] Paulus A, Kammler S, Heuer S, *et al.* Sol gel vs solid state synthesis of the fast lithium-ion conducting solid state electrolyte $Li_7La_3Zr_2O_{12}$ substituted with iron. *J Electrochem Soc* 2019, **166**: A5403–A5409.
[13] Murugan R, Thangadurai V, Weppner W. Fast lithium ion conduction in garnet-type $Li_7La_3Zr_2O_{12}$. *Angew Chem Int Ed* 2007, **46:** 7778–7781.
[14] Kamaya N, Homma K, Yamakawa Y, *et al*. A lithium superionic conductor. *Nat Mater* 2011, **10**: 682–686.
[15] Wada H, Menetrier M, Levasseur A, *et al*. Preparation and ionic conductivity of new B_2S_3-Li_2S-LiI glasses. *Mater Res Bull* 1983, **18**: 189–193.
[16] Aono H, Sugimoto E, Sadaoka Y, *et al.* Ionic conductivity and sinterability of lithium titanium phosphate system. *Solid State Ion* 1990, **40–41**: 38–42.
[17] Xuefu S, Nemori H, Mitsuoka S, *et al*. High lithium-ion-conducting NASICON-type $Li_{1+x}Al_xGe_yTi_{2-x-y}(PO_4)_3$ solid electrolyte. *Front Energy Res* 2016, **4**: 12.
[18] Zhu Y, He X, Mo Y, *et al*. Origin of outstanding stability in the lithium solid electrolyte materials: Insights from thermodynamic analyses based on first-principles calculations. *ACS Appl Mater Interfaces* 2015, **7**: 23685–23693.
[19] Monchak M, Hupfer T, Senyshyn A, *et al.* Lithium diffusion pathway in $Li_{1.3}Al_{0.3}Ti_{1.7}(PO_4)_3$ (LATP) superionic conductor. *Inorg Chem* 2016, **55:** 2941–2945.
[20] Hupfer T, Bucharsky EC, Schell KG, *et al*. Evolution of microstructure and its relation to ionic conductivity in $Li_{1+x}Al_xTi_{2-x}(PO_4)_3$. *Solid State Ion* 2016, **288:** 235–239.
[21] Hupfer T, Bucharsky EC, Schell KG, *et al.* Influence of the secondary phase $LiTiOPO_4$ on the properties of $Li_{1+x}Al_xTi_{2-x}(PO_4)_3$ (x=0; 0.3). *Solid State Ion* 2017, **302:** 49–53.
[22] Rettenwander D, Welzl A, Pristat S, *et al.* A microcontact impedance study on NASICON-type $Li_{1+x}Al_xTi_{2-x}(PO_4)_3$ ($0 \leqslant x \leqslant 0.5$) single crystals. *J Mater Chem A* 2016, **4:** 1506–1513.
[23] Xiao W, Wang J, Fan L, *et al*. Recent advances in $Li_{1+x}Al_xTi_{2-x}(PO_4)_3$ solid-state electrolyte for safe lithium batteries. *Energy Storage Mater* 2019, **19**: 379–400.
[24] Mertens A, Yu S, Schön N, *et al*. Superionic bulk conductivity in $Li_{1.3}Al_{0.3}Ti_{1.7}(PO_4)_3$ solid electrolyte. *Solid State Ion* 2017, **309**: 180–186.
[25] Bucharsky EC, Schell KG, Hintennach A, *et al.* Preparation and characterization of sol-gel derived high lithium ion conductive NZP-type ceramics $Li_{1+x}Al_xTi_{2-x}(PO_4)_3$. *Solid State Ion* 2015, **274:** 77–82.
[26] Waetzig K, Rost A, Langklotz U, *et al.* An explanation of the microcrack formation in $Li_{1.3}Al_{0.3}Ti_{1.7}(PO_4)_3$ ceramics. *J Eur Ceram Soc* 2016, **36:** 1995–2001.

[27] Aono H, Sugimoto E, Sadaoka Y, *et al.* Electrical property and sinterability of $LiTi_2(PO_4)_3$ mixed with lithium salt (Li_3PO_4 or Li_3BO_3). *Solid State Ion* 1991, **47:** 257–264.
[28] Kwatek K, Nowiński JL. Electrical properties of $LiTi_2(PO_4)_3$ and $Li_{1.3}Al_{0.3}Ti_{1.7}(PO_4)_3$ solid electrolytes containing ionic liquid. *Solid State Ion* 2017, **302**: 54–60.
[29] Sharma N, Dalvi A. Dispersion of Li_2SO_4-$LiPO_3$ glass in $LiTi_2(PO_4)_3$ matrix: Assessment of enhanced electrical transport. *J Alloys Compd* 2019, **782:** 288–298.
[30] Kwatek K, Nowiński JL. Solid lithium ion conducting composites based on $LiTi_2(PO_4)_3$ and $Li_{2.9}B_{0.9}S_{0.1}O_{3.1}$ glass. *Solid State Ion* 2018, **322:** 93–99.
[31] Kwatek K, Nowiński JL. The lithium-ion-conducting ceramic composite based on $LiTi_2(PO_4)_3$ with addition of LiF. *Ionics* 2019, **25**: 41–50.
[32] Schön N, Gunduz DC, Yu S, *et al*. Correlative electrochemical strain and scanning electron microscopy for local characterization of the solid state electrolyte $Li_{1.3}Al_{0.3}Ti_{1.7}(PO_4)_3$. *Beilstein J Nanotechnol* 2018, **9**: 1564–1572.
[33] Meertens D, Kruth M, Tillmann K. FEI Helios NanoLab 400S FIB-SEM. *J Large-Scale Res Facil* 2016, **2:** A59.
[34] Luysberg M, Heggen M, Tillmann K. FEI Tecnai G2 F20. *J Large-Scale Res Facil* 2016, **2:** A77.
[35] Kovács A, Schierholz R, Tillmann K. FEI Titan G2 80-200 CREWLEY. *J Large-Scale Res Facil* 2016, **2:** A43.
[36] Dashjav E, Tietz F. Neutron diffraction analysis of NASICON-type $Li_{1+x}Al_xTi_{2-x}P_3O_{12}$. *Z Anorg Allg Chemie* 2014, **640:** 3070–3073.
[37] Mooney RW, Aia MA. Alkaline earth phosphates. *Chem Rev* 1961, **61:** 433–462.
[38] Metwalli E, Brow RK. Modifer effects on the properties and structures of aluminophosphate glasses. *J Non Cryst Solids* 2001, **289:** 113–122.
[39] Moreau F, Durán A, Muñoz F. Structure and properties of high Li_2O-containing aluminophosphate glasses. *J Eur Ceram Soc* 2009, **29:** 1895–1902.
[40] Bearden JA. X-ray wavelengths. *Rev Mod Phys* 1967, **39:** 78–124.
[41] Kanaya K, Okayama S. Penetration and energy-loss theory of electrons in solid targets. *J Phys D: Appl Phys* 1972, **5**: 43–58.
[42] Hultman L, Mitterer C. Thermal stability of advanced nanostructured wear-resistant coatings. In *Nanostructured Coatings.* Cavaleiro A, De Hosson JTM, Eds. New York: Springer, 2006: 480.
[43] Rahaman MN. Ceramic Processing. Boca Raton, US: CRC Press, 2007.
[44] Saidi M, Coffy G, Sibieude F. Les systemes binaires $AlPO_4$–M_3PO_4 (M=Li, Na, K). *J Therm Anal* 1995, **44**: 15–23.